

Flexoelectric-boosted piezoelectricity of BaTiO₃@SrTiO₃ core-shell nanostructure determined by multiscale simulations for flexible energy harvesters



Yeon-gyu Kim ^{a,1}, Hyunseung Kim ^{b,c,1}, Gyoung-Ja Lee ^d, Han-Uk Lee ^e, Sang Gu Lee ^e, Changyeon Baek ^f, Min-Ku Lee ^d, Jin-Ju Park ^d, Qing Wang ^g, Sung Beom Cho ^{e,*}, Chang Kyu Jeong ^{b,c,**}, Kwi-Il Park ^{a,*}

^a School of Materials Science and Engineering, Kyungpook National University, 80 Daehak-ro, Buk-gu, Daegu 41566, Republic of Korea

^b Division of Advanced Materials Engineering, Jeonbuk National University, Jeonju, Jeonbuk 54896, Republic of Korea

^c Department of Energy Storage/Conversion Engineering of Graduate School & Hydrogen and Fuel Cell Research Center, Jeonbuk National University, Jeonju, Jeonbuk 54896, Republic of Korea

^d Smart Structural Safety and Prognosis Research Division, Korea Atomic Energy Research Institute (KAERI), Daejeon 34057, Republic of Korea

^e Convergence Technology Division, Korea Institute of Ceramic Engineering and Technology (KICET), Jinju, Gyeongnam 52851, Republic of Korea

^f Samsung Electro-Mechanics Co., Suwon, Gyeonggi 16674, Republic of Korea

^g Department of Materials Science and Engineering, The Pennsylvania State University, University Park, PA 16802, USA

ARTICLE INFO

Keywords:

Flexoelectricity
Piezoelectricity
Electromechanical coupling
Core-shell nanoparticle
Computational simulation

ABSTRACT

Achieving lead-free piezoelectric nanoparticles with excellent electromechanical responses is in great demand for fabricating nanoscale electronic devices. Recently, the coupling effect of combining flexoelectricity and piezoelectricity has attracted attention as a promising approach to control electromechanical properties. However, the implication of the coupling for the nanoparticles in this regard has been challenging due to its difficulty in controlling and observing the internal strain gradient. In this study, we demonstrate the flexoelectric-boosted electromechanical properties of piezoelectric nanoparticles using an induced built-in strain gradient in heterogeneous core-shell nanostructure. The composition-graded core-shell structure of BaTiO₃@SrTiO₃ nanoparticles enables a significant increment of the effective piezoelectric charge coefficient via the chemical heterogeneities-induced lattice strain gradient. Through the combinations of *ab initio* calculation and multiphysics simulations, the origin of the strain distribution over nanoparticles is theoretically interpreted with accompanying phase balance and diffusion criteria. In addition, our designed core-shell nanoparticles-based energy harvesting devices generate highly efficient and flexoelectric-boosted piezoelectric output signals. Individual core-shell nanoparticles and related elastomeric nanocomposites reported in this work represent state-of-the-art electromechanical properties compared to previously reported piezoelectric nanoparticles and composites. This study provides a new source of inspiration for achieving high-performance lead-free piezoelectric nanostructures, paving the way for developing nano-electromechanical applications.

1. Introduction

Mechanical energy harvesting systems based on various functional materials have been widely studied, as they can convert mechanical to electrical energy *via* piezoelectricity or triboelectricity [1–3]. Especially, piezoelectric nanoparticles (NPs) have advantageous properties for

composite-based electromechanical devices [4–7] because of their distinct physical and chemical properties that use higher inherent surface-to-volume ratio [8–11]. For example, various composite-type piezoelectric energy harvesters have shown high performance as well as simple and cost-effective fabrication. In particular, lead-free piezoelectric NPs have drawn the interest of researchers for manufacturing

* Corresponding authors.

** Corresponding author at: Division of Advanced Materials Engineering, Jeonbuk National University, Jeonju, Jeonbuk 54896, Republic of Korea.

E-mail addresses: csb@kicet.re.kr (S.B. Cho), ckyu@jbnu.ac.kr (C.K. Jeong), kipark@knu.ac.kr (K.-I. Park).

¹ These authors contributed equally to this work.

environmentally friendly and biocompatible devices [12]. Nevertheless, it is challenging to realize lead-free NPs with high piezoelectricity because most high-performance piezoelectric NPs contain lead or rare chemical elements, and complex stoichiometry for phase structures is difficult to control [6,13–16]. To take full advantage of the lead-free piezoelectric NPs and their electromechanical applications, developing not only lead-free but also high-performance piezoelectric NPs through the exploration of nanoscale electromechanical mechanisms becomes urgent and essential [16–18].

The coupling effect between flexoelectricity and piezoelectricity, which is one of the recently debated routes to manipulating piezoresponse, has presented a straightforward strategy to enhance electromechanical properties. In this regard, flexoelectricity refers to strain gradient-induced electric polarization, whereas piezoelectricity is based on uniform strain-induced electric polarization [19,20] that has been considered negligible in bulk dielectric materials. This is because the produced atomistic strain gradient in macroscale systems is generally minute in addition to tiny flexoelectric coefficients [21,22]. In contrast, flexoelectricity manifests its importance in nanoscale systems since the magnitude of strain gradient is inversely proportional to the size of structures [23–27]. Recent studies have reported that the strain gradient in piezoelectric thin films is seven orders of magnitude larger than that in bulk materials, [28,29] and it is associated with various factors, including strain relaxation of epitaxial films, [24,28,30,31] domain walls, [23] and external stimuli (e.g., mechanical bending, laser radiation, nanoscale probe indentation, etc.) [25,27,29,32]. This strain gradient can generate a significant magnitude of flexoelectric-induced electric fields, which bestows the modification of electromechanical properties such as tuning of ferroelectric domain configuration and driving the shift of hysteresis curves [24,31,33–36]. In contrast to the field of thin films, however, little research has been conducted on the flexoelectric-coupling effects on piezoelectricity in the field of NPs despite its vital roles in electromechanical applications. This is mainly due to the difficulty of introducing intrinsic strain gradients in NPs and the limitations of direct observation and theoretical approaches in scalable simulations.

In this study, we demonstrate the flexoelectric-enhanced electromechanical coupling of piezoelectric NPs via a simple synthesis of core-shell structure and theoretical analysis based on multiscale and multi-physics simulation. BaTiO₃-SrTiO₃ core-shell (BT@ST) NPs are introduced by a facile hydrothermal reaction with the well-controlled ST shell thickness. The concentration-graded ST shell layer uniformly formed on the surface of BT core NPs can induce strain gradient in the core-to-surface direction of NPs because of the lattice parameter differences in the perovskite crystal structure. Thus, this nanoscale strain engineering provides a flexoelectric effect, thereby increasing polarization fluctuation in the boosted electromechanical property of a piezoceramic NP. The BT@ST NPs show an approximately 200% increment of effective piezoelectric charge coefficient ($d_{33,\text{eff}}$) by an optimized ST shell thickness compared to the pure BT NPs. Moreover, the structure of core-shell NP and the related strain gradient is investigated through theoretical interpretation via first-principles calculation and multi-physics finite element method (FEM), demonstrating detailed mechanisms of phase transitions under compositionally graded shell layer and comprehended strain distributions over the NP. According to experimental and theoretical results, we have proven that boosted piezoelectric properties of core-shell NPs are based on flexoelectric coupling and further provided application fields for flexible energy harvesters. Our study enriches heterostructure distribution designs on specific NPs, offering a simple yet effective approach to controlling the modulability of piezoelectric NPs for future composite-based devices beyond the traditional nanoscale approaches.

2. Experimental section

2.1. Synthesis of the core-shell nanoparticles

BT@ST NPs were synthesized by a hydrothermal reaction. [37] BT NPs prepared by a solid-state reaction, [38] were dispersed in a solution of 100 mL of deionized water and 8 mL of NH₄OH ($\geq 99.99\%$, Sigma-Aldrich). As a precursor for the shell material of BT@ST NPs, Sr(OH)₂•8H₂O (95%, Sigma-Aldrich) was added to the solution under continuous stirring. The stoichiometric molar ratio of Sr and Ti was 1:1.5. Then, the solution was heated to 80 °C and stirred for 30 min on a hotplate. When Sr(OH)₂•8H₂O was fully dissolved in deionized water, the resultant solution was transferred to a Teflon container, which was subsequently sealed in an autoclave. A hydrothermal reaction was completed at 200 °C for 6–18 h. The resultants collected from an autoclave were washed with deionized water and ethanol several times. Finally, the freeze-drying process was performed to evaporate water from the washing process without agglomeration. Additional milling processes are not needed because the last freeze-drying process prevent any serious agglomeration of NPs.

2.2. Density functional theory calculation

All density functional theory (DFT) calculations were performed using the VASP package [39] using the projector augmented wave method [40]. The Perdew-Burke-Ernzerhof [41] exchange-correlation functional was used. The alloy systems of special quasi-random structures (SQS) [42] were generated with 80 atom supercell using *mcsqs* code of the Alloy Theoretic Automated Toolkit [43]. The plane-wave energy cutoff was set to 520 eV, and Hellmann-Feynman forces were under 0.01 eV·Å⁻¹. The Brillouin zone was sampled using 100 k-points density per 1 Å³ of reciprocal cell. The enthalpy of mixing (ΔH_{mix}) is defined as

$$\Delta H_{\text{mix}}[(\text{Sr}_x\text{Ba}_{1-x})\text{TiO}_3] = E[(\text{Sr}_x\text{Ba}_{1-x})\text{TiO}_3] - (1-x)E[\text{BaTiO}_3] - xE[\text{SrTiO}_3] \quad (1)$$

where x is the molar concentration, $E[(\text{Sr}_x\text{Ba}_{1-x})\text{TiO}_3]$ is the total energy of the SQS structure, $E[\text{BaTiO}_3]$, and $E[\text{SrTiO}_3]$ are the total energies of BT and ST in the ground state. These values can be obtained from the DFT calculations. This enthalpy of mixing can be expressed with a regular solution model [44] for hetero-structural alloy in the form of

$$\Delta H_{\text{mix}}(x) = (1-x)\Delta H_{\text{BT}} + x\Delta H_{\text{ST}} + x(1-x)\Omega \quad (2)$$

where H_{BT} and H_{ST} represent the enthalpies of the endpoints for BT and ST, and Ω represents the regular solution interaction parameters. The ΔS_{mix} is given by

$$\Delta S_{\text{mix}}(x) = -nk_B[x\ln(x) + (1-x)\ln(1-x)] \quad (3)$$

where k_B represents a Boltzmann constant value of 8.617×10^{-5} eV·K⁻¹, and n represents the cation site degeneracy. Gibbs-free energy of mixing, which includes ΔH_{mix} , ΔS_{mix} , and temperature, is given as follows:

$$\Delta G_{\text{mix}}(x, T) = \Delta H_{\text{mix}}(x) - T\Delta S_{\text{mix}}(x) \quad (4)$$

2.3. Finite element method simulation

FEM simulations were performed using COMSOL Multiphysics 5.5 package to model the concentration distribution and induced strain inside NPs. The ion diffusion part is modeled with following Fick's second law,

$$\frac{\partial c}{\partial t} = D \frac{\partial^2 J}{\partial r^2} \quad (5)$$

with the boundary condition of a constant surface concentration. D is the diffusivity obtained from the EDS mapping experiment ($0.25 \text{ m}^2 \cdot \text{s}^{-1}$), c represents the concentration, t represents the time, J is the diffusion flux, and r is the radial distance of the spherical particle. In this boundary condition, the analytic solution is known for $c(x, t) = 1 - \text{erf}\left(\frac{x}{2\sqrt{Dt}}\right)$; thus, we used this form for COMSOL Multiphysics modeling with structural analysis. The lattice mismatch strain that depends on the concentration is defined as

$$\epsilon = \frac{|((1-c)a_{\text{BaTiO}_3} + (c)a_{\text{SrTiO}_3}) - a_{\text{BaTiO}_3}|}{a_{\text{BaTiO}_3}} \quad (6)$$

Simplified equations for a spherically symmetric linear elasticity problem. As usual, a point in the solid is identified by its spherical polar coordinates (R, θ, ϕ). The relationship between the stress and strain is known as $\sigma = C \cdot \epsilon$, where C is the elastic coefficient by called the stiffness tensor, σ and ϵ represent the stress and strain tensor as followed, respectively:

$$\sigma = \begin{bmatrix} \sigma_{RR} & 0 & 0 \\ 0 & \sigma_{\theta\theta} & 0 \\ 0 & 0 & \sigma_{\phi\phi} \end{bmatrix} \quad \epsilon = \begin{bmatrix} \epsilon_{RR} & 0 & 0 \\ 0 & \epsilon_{\theta\theta} & 0 \\ 0 & 0 & \epsilon_{\phi\phi} \end{bmatrix} \quad (7)$$

For spherical symmetry, the governing equation of linear elasticity reduces to

$$\sigma_{RR} = \frac{E}{(1+\nu)(1-2\nu)} \{(1-\nu)\epsilon_{RR} + \nu\epsilon_{\theta\theta} + \nu\epsilon_{\phi\phi}\} - \frac{E\alpha\Delta T}{1-2\nu} \quad (8)$$

ν represents Poisson's ratio, α represents the thermal expansion coefficient, E is Young's modulus, and ΔT is temperature change. Here, we neglected the temperature dependency in the system with $\Delta T = 0^\circ\text{C}$. The stiffness tensor is calculated by density functional perturbation theory with an increased cutoff energy of 800 eV [45]. The young's modulus and Poisson's ratio were extracted from the stiffness tensor [46].

2.4. Fabrication of piezoelectric nanocomposite film

Synthesized BT@ST NPs were dispersed inside the polydimethylsiloxane (PDMS) elastomer (Sylgard 184, Dow Corning, based on curing agent ratio 10:1) matrix in specific proportion (20 wt%) for fabricating a piezoelectric nanocomposite. The nanocomposite was spin-casted onto a PDMS-coated silicon (Si) wafer at a spinning rate of 1500 rpm for 30 s. Next, another PDMS layer was spin-casted on nanocomposite/PDMS/Si substrate and fully hardened at 80°C for 2 h in a convection oven. The hardened PDMS/nanocomposite/PDMS structure was diced into $32 \times 32 \text{ mm}^2$ pieces. Each diced layer was peeled-off and sandwiched between two indium tin oxide (ITO)-coated polyethylene terephthalate (PET) films (Sigma-Aldrich, bottom film: 178 μm , top film: 127 μm) to characterize the energy conversion performance of nanocomposites. Subsequently, copper (Cu) wires were connected to two electrodes by conductive epoxy (Chemtronics, CW2400) to detect electric output signals. The final device was poled for 3 h at 100°C under an external applied voltage of 1.5 kV. In addition, a thick bulk-type nanocomposite was also fabricated for characterizing electric and piezoelectric properties. BT@ST NPs-dispersed PDMS was poured into a petri-dish and fully cured at 80°C for 2 h in a convection oven. The hardened bulk nanocomposite was diced into pieces with a diameter of 25 mm.

2.5. Material characterization

Morphologies of synthesized BT@ST NPs were analyzed by field-emission scanning electron microscopy (SEM, SU8220, Hitachi, Japan) and transmission electron microscopy (TEM, Titan G2, FEI Company, USA) with EDS. The crystallographic structure of the perovskite BT@ST

NPs was characterized by X-ray diffraction (XRD, EMPYREAN, PANalytical, UK). Raman microscope (Renishaw, inVia reflex, UK) with the 523-nm line of an Ar⁺ laser was also used to comprehensively analyze the phase of BT@ST NPs. Some device structures were also analyzed by the Field Emission SEM (SUPRA40VP, Carl Zeiss) installed in the Center for University-wide Research Facilities (CURF) at Jeonbuk National University.

2.6. Measurement of piezoelectric response of BT@ST NP

The piezoelectric properties of each single BT@ST NP were characterized by a piezoresponse force microscopy (PFM) and demonstrated by atomic force microscopy (AFM, Park Systems, NX20, South Korea) with a conductive probe (Budget Sensors, ElectriMulti75-G, Bulgaria). From the PFM amplitude curve and phase hysteresis loop acquired when a DC voltage ranging from -10 to 10 V with a superimposed AC voltage of 10 V amplitude were applied to the selected top of a single BT@ST NP, the $d_{33,\text{eff}}$, which generated polarization per unit stress-induced in an out-of-plane direction, of piezoelectric NPs, was determined.

2.7. Measurement of electric and piezoelectric properties of BT@ST NPs-based nanocomposite

To investigate the polarization-electric field ($P-E$) hysteresis behavior of BT@ST NP-based nanocomposites, Ag-based electrodes (conductive epoxy, Chemtronics, CW2400) with a diameter of approximately 8 mm were formed on the top and bottom surface of the coin-shaped nanocomposite film with a thickness of 2.5 mm and a diameter of 8.5 mm. The optimal hysteresis loop was acquired using a ferroelectric tester (TF analyzer 2000, aixACCT, Germany) at a maximum electric field of $150 \text{ kV} \cdot \text{cm}^{-1}$ with 1 Hz. For exploring the leakage current behaviors of BT@ST NPs-embedded nanocomposites from current density-electric field ($J-E$) characteristics, Cu electrodes with a diameter of 300 μm were deposited onto the nanocomposite placed on flat aluminum plates with a thermal evaporator (VEV-503, Scientific Engineering, South Korea). The top and bottom electrodes were connected to a voltage source (6487, Keithley, USA) to apply the electric field ranging from -10 to 10 $\text{kV} \cdot \text{cm}^{-1}$; simultaneously, the leakage current signals were measured using a picoammeter (6487, Keithley, USA). For characterizing the dielectric properties of a nanocomposite sandwiched between two electrodes, the dielectric constant and loss tangent with frequencies ranging from 1 kHz to 1 MHz using an LCR meter (4284 A, Hewlett Packard, USA) with a dielectric test fixture (16451B, Hewlett Packard, USA). The piezoelectric charge coefficient (d_{33}) of BT@ST NP-dispersed nanocomposite was calculated from the average value of the measured data of more than 20 different points from the center to the outside of samples using a d_{33} meter (YE2730A, SINOCERA, China). For measuring the piezoelectric output signals harvested from nanocomposites sandwiched between two ITO-coated plastic substrates, a programmable bending machine (Bending Machine System, SnM, South Korea) was used to induce alternative and regular mechanical bending deformations with an effective strain of 30% and strain rate of 30-s^{-1} . The output voltage and current signals generated by repeatedly bending of nanocomposites were detected using a sourcemeter (2611 A, Keithely, USA) and acquired simultaneously on a computer.

3. Results and discussion

Fig. 1a illustrates the experimental setup for the synthesis of BT@ST NPs. The compositionally graded shell layer, where Sr concentration is gradually declined from the surface to the core, is continuously formed on the original pure BT NPs with an average diameter of 400 nm. The formation of this gradient core-shell structure results from the Kirkendall effect, with the simultaneous interdiffusion of Sr²⁺ and Ba²⁺ cations.[37,47,48] Note that although BaTiO₃@(Sr_xBa_{1-x})TiO₃ core-shell structure NP is used, the main A-site cation of the perovskite crystal

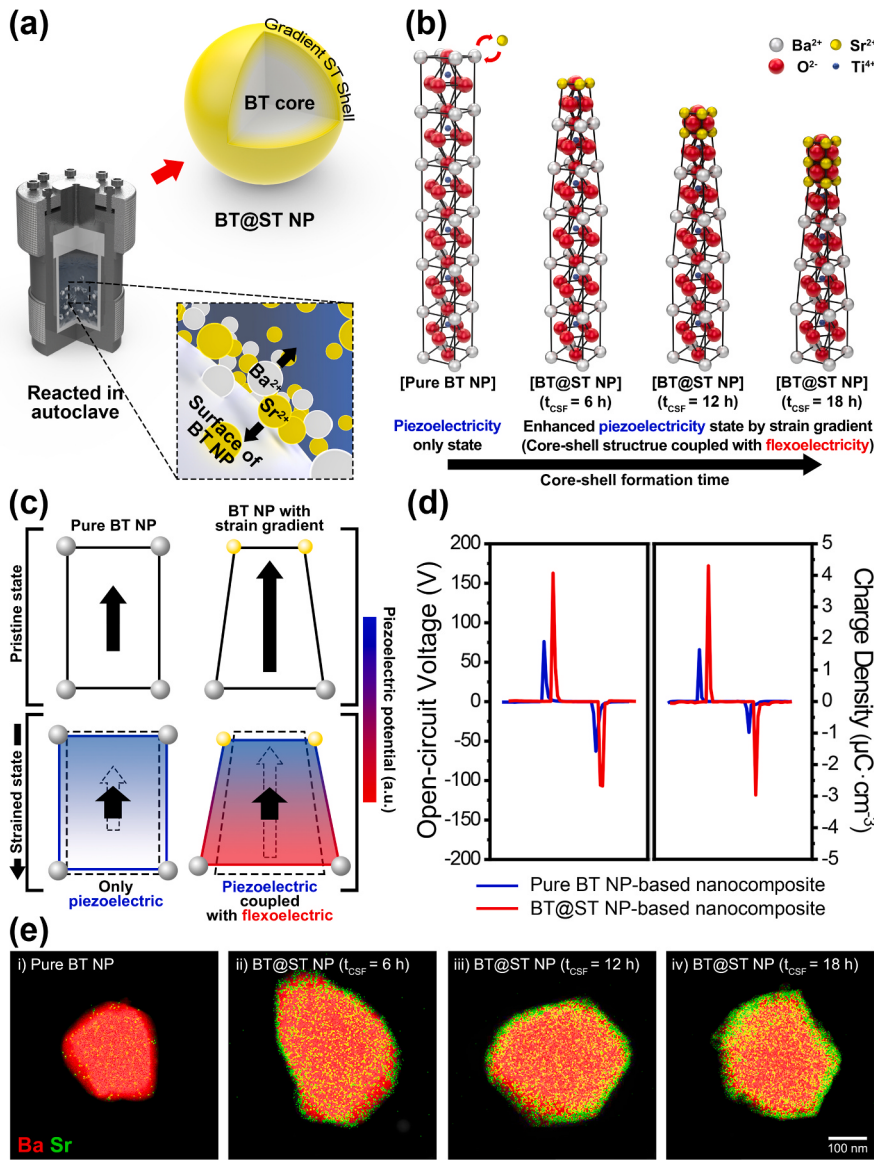


Fig. 1. (a) Schematic illustrations for forming the gradient ST shell on the surface of pure BT NPs *via* a hydrothermal reaction. The magnified image shows the simultaneous interdiffusion process of Ba^{2+} and Sr^{2+} cations during the hydrothermal reaction. (b) Schemes showing the dependence of the induced strain gradient on the extent of ST shell change in various reaction times. The flexoelectricity-coupled core-shell structure can provide the extrinsic strain gradient inside the lattice BT@ST NPs, improving piezoelectricity. (c) Schematic illustrations of the comparison of piezoelectric potential difference that could be generated inside the lattice of the pure BT NP and core-shell NP under pristine and stressed states. Compared to the piezoelectricity-based BT NP, flexoelectricity-coupled BT@ST NP can produce high piezo-potential distribution due to the induced strain gradient from the lattice parameters mismatch of Ba^{2+} and Sr^{2+} cations. (d) Output open-circuit voltage signals and charge density measured from fabricated nanocomposites made of pure BT and BT@ST NPs under mechanical bending and unbending motions. Improved output performance was achieved by adopting BT@ST NPs in a piezoelectric energy device. (e) TEM images and corresponding EDS mapping of pure BT and BT@ST NPs with different t_{CSF} . Ba and Sr contents are indicated as red and green, respectively.

on the shell part is Sr^{2+} , so it can be referred to as BT@ST for simplicity. In addition, note that it is hard to see discrete interface between the BT core and the ST shell due to the multiple phases of shell synthesized continuously [37,47,48]. The overall size of NPs is preserved during the formation of the shell layer because the BT core shrinks, whereas the shell layer thickens. The detailed synthesis step is described in the Experimental Section and Fig. S1. Fig. 1b atomically depicts the process of ST shell formation from the surface of BT NP with the interdiffusion and phase transition according to core-shell formation time (t_{CSF}). The difference in ionic radius of substituted A-site cations in perovskite crystal structures (1.32 Å and 1.49 Å for Sr^{2+} and Ba^{2+} , respectively) [49] causes the lattice parameter fluctuation in the outer shell part of BT@ST NP, resulting in strain gradient-induced electrical polarization (i.e., flexoelectricity) *via* the contribution of Vegard effect [50], in addition to the original piezoelectric BT. Although pure ST has a centrosymmetric perovskite structure (cubic phase, $\text{Pm}\bar{3}\text{m}$), concentration gradient-induced flexoelectricity further distorts the non-centrosymmetric structure of BT (tetragonal phase, $\text{P}4\text{mm}$) and enhances the piezoelectricity of BT@ST NP because of the more facilitated dipole displacement [21,22,51]. This concept of flexoelectric-boosted electromechanical coupling effect is shown in Fig. 1c. Through the contribution of built-in strain gradient, which has

synergistic interactions with piezoelectricity, the BT@ST NP shows a greater polar structure than the pure BT NP [23,26]. Thus, the BT@ST NP could exhibit superior piezoelectric responses when mechanical stress is applied [52–54]. Although the cubic BT phase may be formed on the surface of pure BT NPs as a very thin layers, the lattice difference between cubic and tetragonal BT phases is too small to induce effective strain gradient [55,56], in contrast to BT@ST core-shell structures. Moreover, the surficial layer of the cubic BT phase on the pure BT NPs very few exists and is hard to be controlled. In this regard, flexoelectricity induced in the pure BT NP is negligible. To validate our design for boosted piezoelectric performance, we fabricated piezoelectric nanocomposites made of BT and BT@ST NPs, respectively; subsequently, we measured the output potential difference (open-circuit voltage) and charge density signals generated from the composite-based piezoelectric devices under mechanical bending stress (Fig. 1d). It is shown that the BT@ST NP-based generator produces approximately 200% more enhanced output signals than the pure BT NP-based generator. A more rigorous consideration of generator devices in terms of the characterization of the flexible piezoelectric composite prepared by dispersing BT@ST NP inside polymeric matrix will be discussed in subsequent parts.

Intriguingly, the electromechanical coupling effect of BT@ST NP did

not increase proportionally as the thickness of the shell layer increased. With the introduction of the core-shell structure on the NP, initially (i.e., $t_{CSF} = 6$ h), drastic enhancements in piezoelectric responses were produced because of the flexoelectric-boosted effect. As t_{CSF} increases to 12 or 18 h, however, the piezoelectric responses of BT@ST NPs decrease again. This variation in electromechanical coupling can be explained by the increasing ST part in the shell layer. As t_{CSF} further increased after 6 h, excessive Sr diffused into the NP, inducing the thicker pure ST phase on the shell (see Fig. 1b). This behavior is well demonstrated by TEM-energy dispersive spectroscopy (TEM-EDS) mapping, as shown in Fig. 1e. Notably, Ba was uniformly distributed in the pure BT NP; whereas the detected Sr element is considered a level of noise (Fig. 1e-i). After 6 h of t_{CSF} , Sr concentration significantly increases on the shell, while Ba is depleted in the edge of the NP (Fig. 1e-ii). At this stage, the strain gradient-based flexoelectric coupling is effective on the

piezoelectricity of NPs. The Sr-enriched shell layer becomes thicker by longer reaction time, whereas the overall size of the NP is mostly preserved (Fig. 1e-iii and -iv). Because pure ST is not piezoelectric material, the non-electromechanical property of ST can be more dominant than the flexoelectric-boosted coupling effect in the case of thicker ST shell layers. In addition, the much more diffused Sr into the BT core part can probably reduce the strain gradient and the related flexoelectric effect. This is the reason why the generator device fabricated using BT@ST NPs with thicker ST shell layers shows lower piezoelectric performance than that made of the BT@ST NPs with thinner ST shell layers.

The structure of BT@ST NPs was further quantitatively evaluated on the basis of the EDS mapping and line scan profile (Fig. S2); subsequently, the change in the total Sr/Ba components and the thickness of the ST shell layer as a function of t_{CSF} were plotted in Fig. 2a. The total amount of Sr in BT@ST NPs increases gradually from 4.06 at% for the

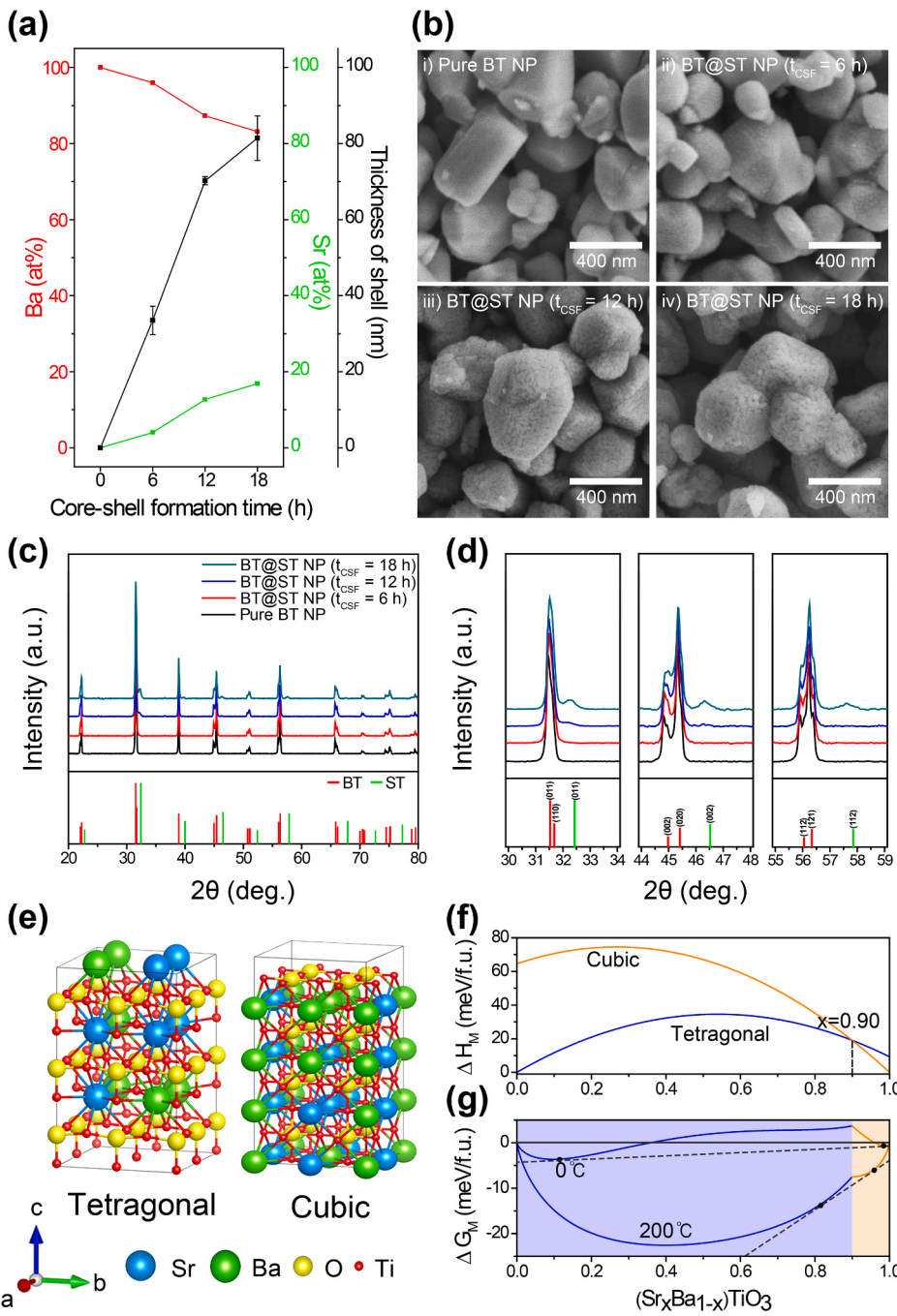


Fig. 2. (a) Graph specifying the change in the amounts of Ba^{2+}/Sr^{2+} cations, and shell thickness as a function of the hydrothermal reaction times. (b, c) SEM images (b) and XRD patterns of pure BT and BT@ST NPs with different t_{CSF} . (d) Detailed XRD patterns 30° – 34° , 44° – 48° , and 55° – 59° to compressively characterize the crystallinity of synthesized NPs. The red and green lines in the bottom panel represent the reference peak positions of BT and ST, respectively. (e) Atomic structure of $(Sr_xBa_{1-x})TiO_3$ alloy systems for tetragonal and cubic structures. The blue, green, yellow, and red atoms represent Sr, Ba, O, and Ti, respectively. (f) The enthalpy of mixing is a function of the molar concentration for tetragonal and cubic phases. The blue and orange lines represent the tetragonal and cubic phases, respectively. (g) The effect of temperature on the Gibbs-free energy of mixing of $(Sr_xBa_{1-x})TiO_3$ alloy systems at 0 and 200 °C. The blue and orange lines represent the tetragonal and cubic phases, respectively. The black dashed line represents a zero value of the Gibbs-free energy of mixing. The common tangent lines and contact points represent gray lines and black markers, respectively.

6 h of t_{CSF} to 16.85 at% for the 18 h of t_{CSF} , where the amount of Ba correspondingly decreases. The thickness of the ST shell is defined as the region with a rapidly increasing Sr content. It is found that the ST shell regime contains approximately 80 at% Sr compared to Ba. The thickness of the ST shell layer increases from 33.5 to 81.4 nm according to the increment of t_{CSF} .

The overall size and morphologies of NPs were also confirmed by SEM. Fig. 2b represents SEM images of pure BT and BT@ST NPs with their t_{CSF} conditions. The pure BT NPs are exhibited spherical or ball milled-polyhedron shape with an average diameter of 400 nm. In addition, the surface morphology of BT@ST NPs is changed to a slightly fleece-like shape as the reaction time increases compared to pure BT NPs. This is presumably due to the Kirkendall effect caused by ionic

exchanges [57,58]. The average size of NPs did not show significant changes, showing an average size of 400 nm even after t_{CSF} of 18 h. The low-magnified SEM images are also presented in Fig. S3 to show the average size of NPs. Fig. 2c shows a series of XRD patterns from pure BT and the BT@ST NPs with their t_{CSF} conditions. The bottom panel presents the reference positions of BT and ST peaks. All NPs show well-synthesized perovskite crystal structures, and this has been demonstrated via Raman spectroscopy (Fig. S4 for Raman spectra obtained from pure BT and BT@ST core-shell NPs) [59]. To investigate detailed changes for each NP, high-resolution XRD patterns are inspected at 2-theta angles 30–34, 44–48, and 55–59, respectively, as presented in Fig. 2d. The XRD pattern of the pure BT NP corresponds to the typical result that shows the tetragonal phase of perovskite crystals. As

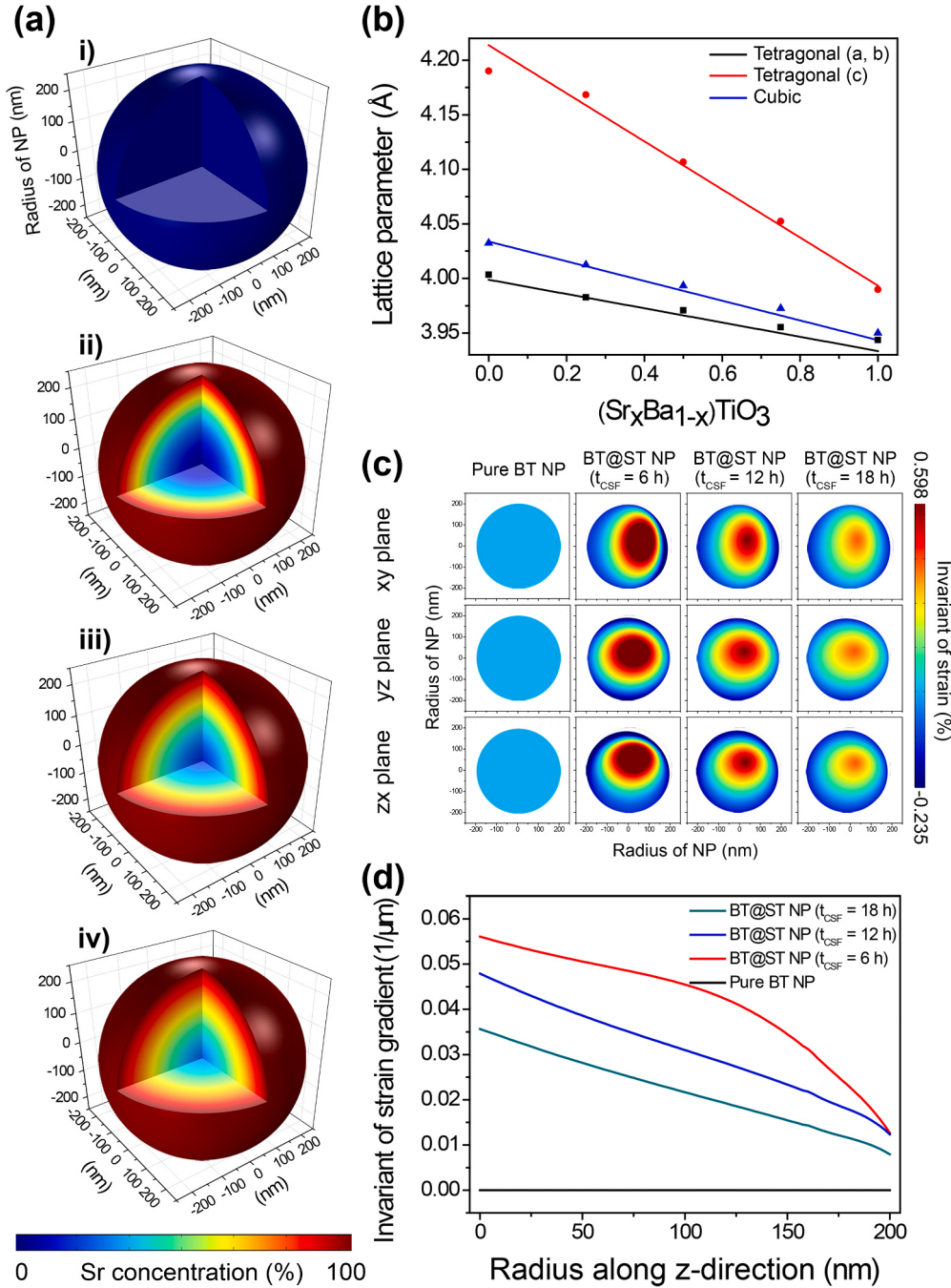


Fig. 3. The distribution of Sr ion with (i) $t_{\text{CSF}} = 0 \text{ h}$, (ii) $t_{\text{CSF}} = 6 \text{ h}$, (iii) $t_{\text{CSF}} = 12 \text{ h}$, and (iv) $t_{\text{CSF}} = 18 \text{ h}$. (b) The lattice parameter of $(Sr_xBa_{1-x})TiO_3$ alloys. (c) 2D projection of internal strain invariant of BT and BT@ST NPs. (d) The gradient of the invariant of the strain along z-direction.

t_{CSF} increases, the overall XRD peaks shift to higher angles, indicating that NPs have smaller lattice parameters. Importantly, no ST phase peak is found in NPs with a t_{CSF} of 6 h. It means that the shell layer does not consist of a uniform ST phase but is composed of compositionally graded multiple phases with a strain gradient. In contrast, in NPs with a t_{CSF} of 18 h, the additional shoulder peaks and the peak shifting appear at the referred position of pure ST peaks. This indicates that as t_{CSF} increases, the shell layer largely becomes the pure ST of cubic phase. These results match our material designs and experimental predictions for flexoelectric-boosted piezoelectric NPs, as aforementioned.

To understand the phase transition mechanism and electromechanics of NPs, we performed DFT calculations for $(Sr_xBa_{1-x})TiO_3$ alloy systems. The detailed calculation method was described in Experimental Section. The alloying behavior and phase competition of cubic and tetragonal phases are calculated using special quasi-random structures [42] to describe the random occupation of Sr^{2+}/Ba^{2+} cations at the A site of the perovskite, as shown in Fig. 2e. The atomic structures of pure ST and BT are represented in Fig. S5. Combining with regular solution model [44], we calculated the enthalpy of mixing as a function of the molar concentration of Sr in the $(Sr_xBa_{1-x})TiO_3$ alloys as shown in Fig. 2f. The tetragonal phase is more stable in most regions, but when the concentration of Sr exceeds 90%, the cubic phase becomes thermodynamically more stable. To understand phase competition behavior during core-shell formation, we also calculated the Gibbs-free energy of mixing at hydrothermal temperatures, as shown in Fig. 2g. The Gibbs-free energy of the mixing is negative for all regions and both phases under 200 °C, which means that alloying is spontaneous during core-shell formation condition. As the t_{CSF} of the hydrothermal process increases, more Sr diffuses, forming an alloy structure. When the concentration exceeds $x = 82\%$, the common tangent point of the Gibbs-free energy for both phases is reached, and the cubic phase can be stably presented with mixed phases. In addition, Sr concentration increase up to 92%, pure cubic is only the thermodynamically stable phase, and the electromechanical properties will be degraded drastically. This result is consistent with the XRD patterns that showed cubic phases as the t_{CSF} increases.

We also performed multiphysics FEM simulation to understand the diffusion behavior and its electromechanical effect more quantitatively. Fick's second law is solved with the diffusivity parameter that is fitted to the result of EDS mapping. Fig. 3a shows the distribution of Sr^{2+} ions at each t_{CSF} . Sr^{2+} ions are diffused from the surface region, where there is a concentration gradient. The concentration of Sr^{2+} is high near the surface region and relatively low at the core region. The maximum of the gradient is at $t_{CSF} = 6$ h. Afterward, the concentration difference between the shell and core gradually decreases because Sr^{2+} diffusion reaches the core region of NPs. The calculated Sr concentration as a function of the radius of NPs is well corresponded with the EDS mapping data at each sample, as shown in Fig. S6. This concentration gradient introduces a gradually decreasing lattice parameter because of the difference in ionic radii of Sr^{2+} and Ba^{2+} . It should be noted that the $BaTiO_3 @ (Sr_xBa_{1-x})TiO_3$ core-shell concentration was strictly applied according to the hydrothermally diffusion-based real experiments. We also calculated the lattice parameter as a function of Sr concentration using DFT calculation, as shown in Fig. 3b. The tendency of the lattice parameter is close to the Vegard effect, and this lattice parameter difference introduces the strain boundary condition inside the NP. Combining this diffusion equation and structural mechanics, we performed multiphysics simulation on spherical NPs and evaluated the internal strain invariant as shown in Fig. 3c. Although their patterns are different along the axes due to the anisotropy of the tetragonal phase, the strain invariant gradually decreases as $t_{CSF} = 6$ h. This is because the concentration difference reaches the maximum at $t_{CSF} = 6$ h and gradually decreases again. Such strain invariant distribution also includes the strain gradient, which drives flexoelectric polarization. As a representative case, Fig. 3d shows the gradient of invariant strain along the z-direction (see also Fig. S7). There is no flexoelectric contribution with pure BT NP, but it reaches to the maximum to BT@ST NP after t_{CSF} of 6 h

and gradually decreases as more Sr^{2+} reaches to the core region.

To experimentally verify the correlation between flexoelectricity and piezoelectricity, the microscopic electromechanical behaviors of each NP were evaluated using the switching spectroscopy PFM (SS-PFM), as shown in Fig. 4a [60,61]. The series of amplitude versus DC voltage loops were measured by applying DC voltage from -10 to 10 V with a superimposed AC modulation voltage to a fixed conductive tip on each NP surface; the detailed method for piezoelectric response was described in Experimental Section. Notably, the butterfly-shaped amplitude curves, which represent thin-shelled BT@ST NP after t_{CSF} of 6 h, exhibit substantially larger electromechanical responses than thicker-shell BT@ST and pure BT NPs. As expected from the aforementioned theoretical designs and multiscale computations, the butterfly loops of BT@ST NP with increasing t_{CSF} enable the re-diminution of electromechanical response. A full set of amplitude and phase signals for each pure BT and BT@ST NP is also represented in Fig. S8. From the amplitude curves, the extracted $d_{33,eff}$ summarized in Table S1 and plotted in Fig. 4b. They were quantified as 24.9, 49.6, 29.2, and 23.8 pm·V⁻¹ for pure BT and the BT@ST NPs after 6, 12, and 18 h t_{CSF} , respectively. To further determine the flexoelectric-boosted effect on BT@ST NP at a macroscale, we fabricated the bulk-scale nanocomposites consisting of NP fillers-embedded elastomeric PDMS matrix [4]. To measure the macroscopic d_{33} , we used a quasi-static method, which is known as the Berlincourt method [62], on nanocomposites (Fig. 4b). We obtained the maximum d_{33} of 118 pC·N⁻¹ from thin-shelled BT@ST NP-based nanocomposite (in t_{CSF} of 6 h). In both approaches for measuring piezoelectric responses, the BT@ST NP in t_{CSF} of 6 h shows the highest electromechanical coupling by the flexoelectric-boosted piezoelectric effect. Consequently, a well-matching behavior relationship between $d_{33,eff}$ and macroscopic d_{33} is observed, which corresponds to the theoretical and experimental material design for high-performance electromechanical NPs.

The microscopic and macroscopic piezoresponses of our developed thin-shelled BT@ST NP (t_{CSF} of 6 h) are compared with up-to-date reported piezoelectric NPs and polymer-matrix composites, as shown in Fig. 4c and d (see also Tables S2 and S3). The $d_{33,eff}$ of BT@ST NP in this work is superior to those of well-known perovskite piezoceramic NPs [63–69]. The macroscopic d_{33} of BT@ST NPs-embedded nanocomposite is also much higher than most of the reported piezoelectric nanocomposites [70–80]. Note that the 20 wt% of our experimental condition for composites is based on the previously reported optimum conditions [81–83]. In addition, excessively high contents of BT@ST NP fillers induced dielectric breakdown and current leakage during poling processes. These comparison results show that the optimized BT@ST NP exhibits superior electromechanical characteristics among various piezoelectric NPs because of the theoretically designed coupling effect of flexoelectricity and piezoelectricity.

To evaluate the ferroelectric properties of each BT@ST NP, polarization hysteresis curves of nanocomposites fabricated by BT@ST NPs as well as BT NPs were measured. The detailed methods for ferroelectric properties were described in Experimental Section. Fig. 4e shows the remanent polarization of each nanocomposite. Although overall values and differences are relatively small due to the influence of polymeric PDMS matrix, the maximum remanent polarization value of 0.0146 μ C·cm⁻² is discovered from the thin-shelled BT@ST NP-based nanocomposite (in t_{CSF} of 6 h). This is because the maximized flexoelectric-associated coupling can show the highest polarization in ferroelectric properties [32,36,84,85]. All plots representing the polarization hysteresis curves are presented in Fig. S9. The inset of Fig. 4e shows the leakage current levels of nanocomposites consisting of each NP. In composite materials, an electrical breakdown can easily occur because of the difference in dielectric constants at the interface between the two materials and the concentrated electric field in filler particles. When the electric field reaches the dielectric breakdown threshold, the accumulated charge in ferroelectric fillers should be discharged to the outside [86]. The leakage current level of thin-shelled BT@ST NP-based

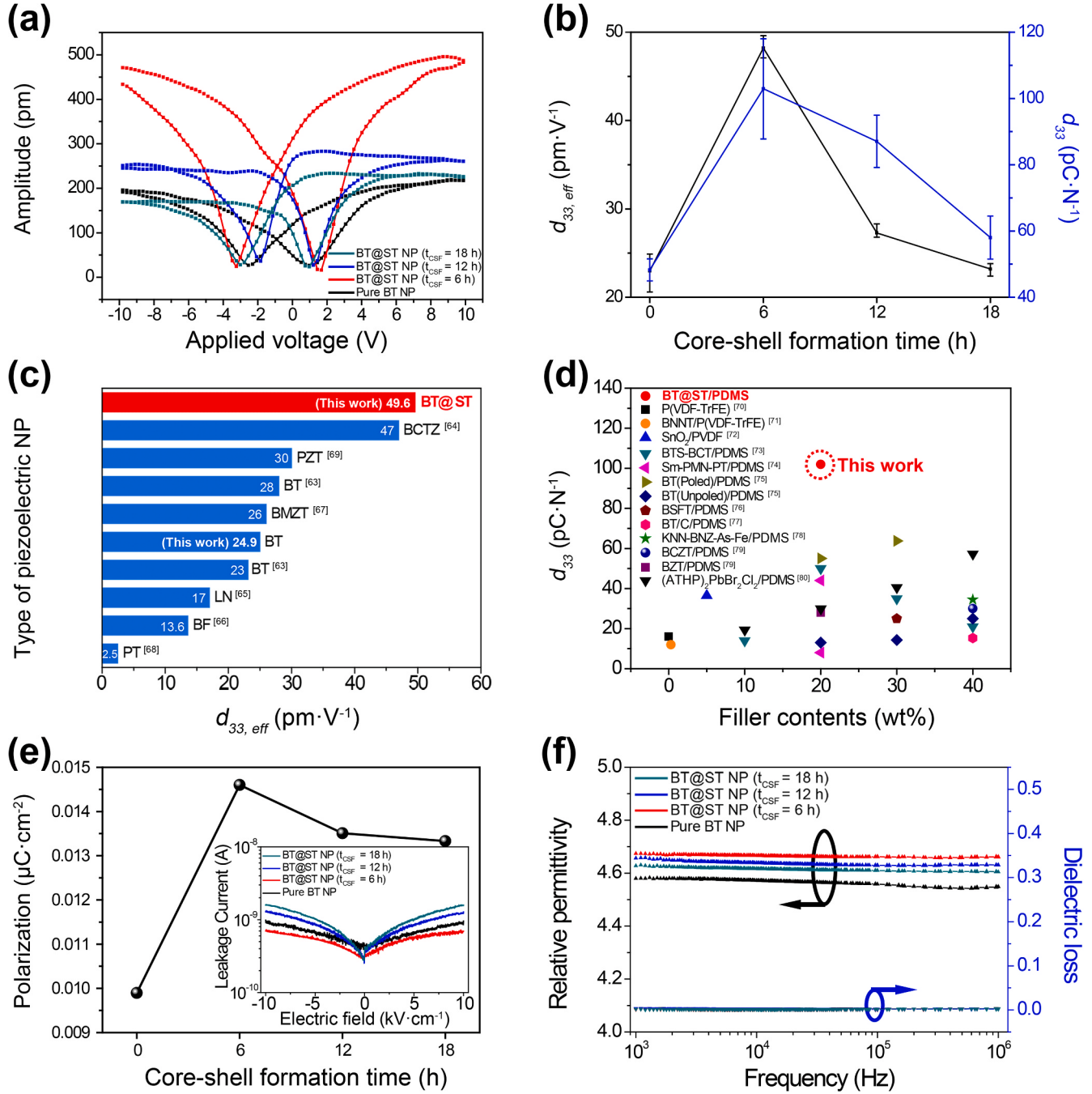


Fig. 4. (a) Variations of piezoelectric response of pure BT and BT@ST NPs with different t_{CSF} , as represented by PFM amplitude under an applied voltage. (b) The $d_{33,eff}$ (black line) of single NP and d_{33} (blue line) of nanocomposites made of NPs, as a function of t_{CSF} . The $d_{33,eff}$ and d_{33} were characterized by a PFM and d_{33} meter, respectively. (c, d) The comprehensive comparison of $d_{33,eff}$ (c) and d_{33} (d) of pure BT and BT@ST NP synthesized in this study with previously reported piezoelectric NPs. Data of (d) are plotted against contents of piezoelectric NPs dispersed inside the polymeric matrix. (e) The remnant polarization of nanocomposite film was obtained at the optimal electric field as a function of t_{CSF} . The inset shows the $J-E$ characteristics for investigating the leakage current behavior of nanocomposites made of hydrothermally synthesized NPs with various t_{CSF} . (f) Frequency dependence of relative permittivity and dielectric loss of nanocomposites made of pure BT and BT@ST NPs.

nanocomposites (in t_{CSF} of 6 h) is lower than that of pure BT NP-based nanocomposites. This is because the thin paraelectric ST shell around the ferroelectric BT core acts as an additional electrical potential barrier that can mitigate the concentration of an electric field and prevent resultant discharging events toward dielectric breakdown [87]. In contrast, interestingly the leakage current levels of thicker-shelled BT@ST NPs-based nanocomposites (in 12 and 18 h t_{CSF}) are higher than that of pure BT NP-based nanocomposites. This is because NPs with thick shells and a dielectric constant that changes from the center of the

particle to the shell can cause greater leakage currents with discontinuous changes in the local electric field at the interface [88]. An opposite trend is because the thicker paraelectric ST shell around NPs becomes dominant to create current paths compared to ferroelectric BT cores, causing more electrically conductive properties within the nanocomposites [89]. As shown in Fig. 4f, the series of relative permittivity of the nanocomposites were measured with high resolution. The dielectric properties are also affected by the flexoelectricity-based coupling effect that can be improved by changes in the internal domain structure due to

dielectric constant and strain gradient [90,91]. Although the overall level of dielectric constants is not high due to the strong effect of the PDMS matrix, the thin-shelled BT@ST NP-based nanocomposites (in t_{CSF} of 6 h) show the highest permittivity. The thicker-shelled BT@ST NP-based nanocomposites demonstrated re-decreasing dielectric constants. This tendency corresponds to flexoelectric-boosted coupling effects. Because flexoelectricity can increase the dielectric constant, the thin-shelled BT@ST NPs induce slightly higher permittivity in the composite configuration. Note that dielectric loss factors of all composites are low and the same due to the polymer matrix.

To investigate the electrical outputs harvested from the designed BT@ST NPs, we fabricated nanocomposite-based flexible devices by adopting the simple and low-cost spin-casting method [4,13,81], as illustrated in Fig. 5a. The mixture of NPs and PDMS prepolymer liquid was spin-casted on a Si substrate. After curing the nanocomposite, it was peeled-off and sandwiched between top and bottom ITO electrode-deposited PET sheets. In this step, nanocomposites were firmly

attached by additional pre-cured hard PDMS. Processing details for the flexible nanocomposite-based device were provided in the Experimental Section. Fig. 5b shows the picture of real nanocomposite packaged with two plastic substrates that can be bent with fingers. Fig. 5c shows cross-sectional SEM images of the nanocomposite-based electromechanical device, where NPs are well distributed inside the PDMS matrix (the inset of Fig. 5c). We characterized the electrical output performance of flexible electromechanical nanocomposites converted by mechanical bending deformation. Fig. 5d and e, respectively, show the output open-circuit voltage and short-circuit current signals generated from each piezoelectric nanocomposite consisting of different types of NPs. As expected by the flexoelectric-boosted coupling effect, the electromechanical nanocomposite fabricated using the thin-shelled BT@ST NPs (in t_{CSF} of 6 h) shows superior switched signal peaks (open-circuit voltage of ~160 V and short-circuit current of ~700 nA). In contrast, piezoelectric nanocomposites consisting of pure BT NPs produce the smallest open-circuit voltage and short-circuit current signals because

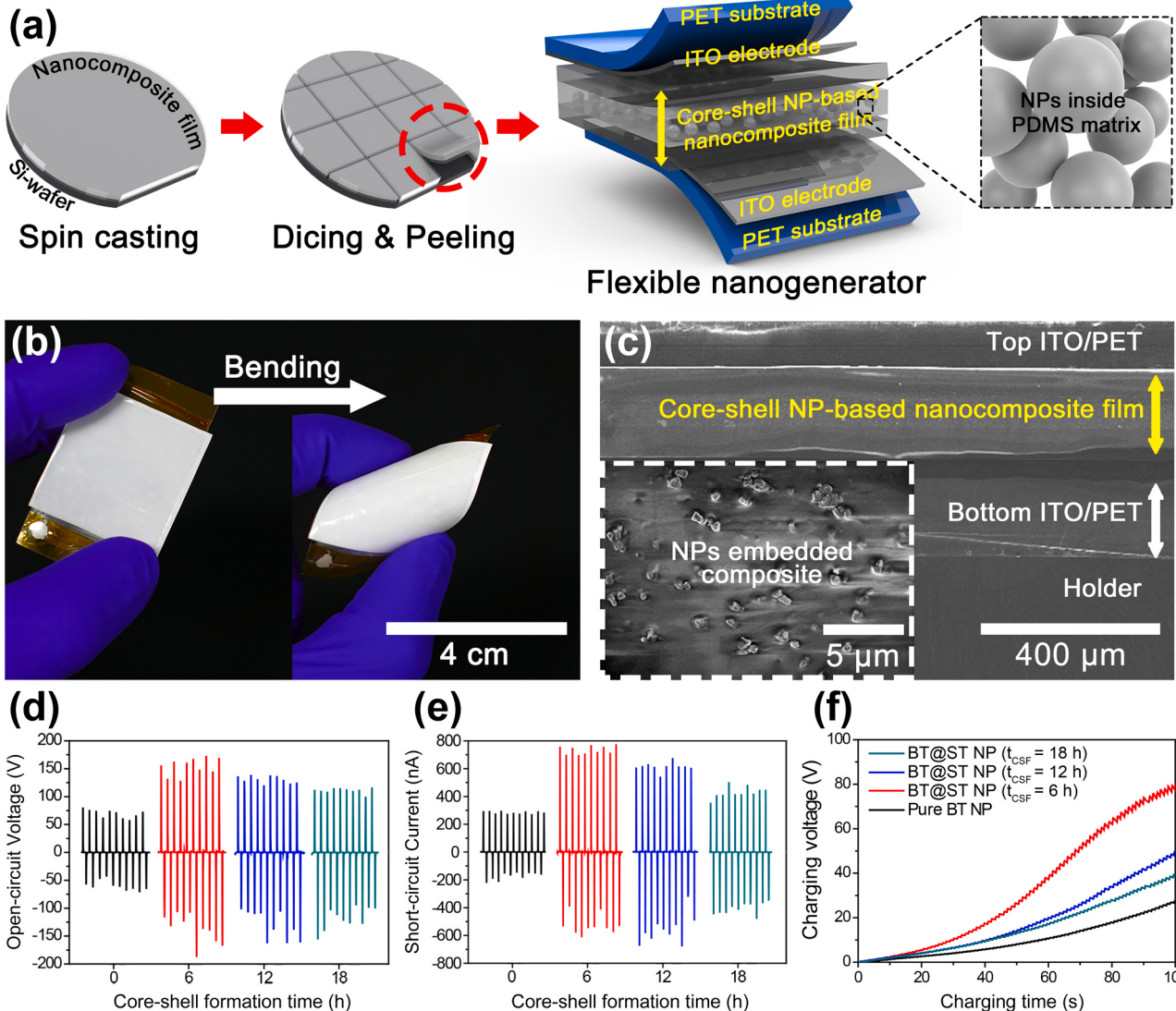


Fig. 5. (a, b) Schematic illustration (a) and real photograph (b) of NPs-embedded nanocomposites sandwiched between the two ITO-coated plastic substrates to characterize piezoelectric output performance. The right panel of (b) showing the fabricated sample bent by human fingers confirms that nanocomposite is sufficiently mechanically stable and flexible during repeatedly bending motions. (c) The cross-sectional SEM images of the nanocomposite layer between the top and bottom plastics (the inset: a magnified image). (d, e) Output open-circuit voltage (d) and short-circuit current signals (e) generated from nanocomposites based on pure BT and hydrothermally synthesized BT@ST NPs when subjected to periodically bending and unbending motions (black: pure, red: $t_{CSF} = 6$ h, blue: $t_{CSF} = 12$ h, and green: $t_{CSF} = 18$ h). (f) The charging curve of a supercapacitor (capacity: 104 nF) driven using the generated electricity from nanocomposites deformed repeat bending.

the built-in strain gradient-based flexoelectric effect is not in pure BT NPs. To demonstrate that the measured signals were purely generated from the electromechanical NPs, switching polarity tests were also performed (Fig. S10) [92,93]. Inverse peak polarity with the same level was observed in the test, indicating that the output signals of nanocomposite devices are originated from charges generated by the piezoelectricity of NPs without other artifacts [94,95]. As shown in Fig. 5f, the thin-shelled BT@ST NPs-based nanocomposite rapidly charges the capacitor to 80 V.

4. Conclusions

In conclusion, we have demonstrated the flexoelectric-boosted piezoelectric coupling effect of BT@ST NPs induced by nanoscale built-in strain gradient, which is verified by multiscale simulations as well as experimental designs. With adequate ST shell thickness, the piezoresponse of BT@ST NPs was efficiently enhanced by the improved oscillation of polarization via strain gradient-induced flexoelectricity within the lattice. In contrast, the thicker-shelled BT@ST NPs showed re-lowered piezoelectric properties because of the dominant effect of the paraelectric ST layer and reduced strain gradient. We have investigated the physical properties of core-shell NPs using not only piezoelectric measurement approaches but other electrical analyses, including dielectric, ferroelectric, and leakage measurements, as well as material characterizations. In addition, the strain gradient within core-shell NPs has been deeply verified and computed using multiscale and multi-physics simulations, including FEM and DFT calculations on diffusion, structural mechanics, and phase competition. Our developed electromechanical core-shell NPs and related nanocomposites demonstrated state-of-the-art piezoelectric properties among up-to-date reported individual NPs. The flexible nanocomposite consisting of optimized BT@ST NPs and polymer matrix generates highly efficient and flexoelectric-boosted piezoelectric output signals as an energy generator for capacitor charging. This study proves the physical phenomena of flexoelectric and piezoelectric interactions in NPs. Furthermore, we have paved the unique way to improve nanoscale electromechanical coupling for future research on piezoelectric device performance.

CRediT authorship contribution statement

Yeon-gyu Kim: Conceptualization, Methodology, Investigation, Formal analysis, Writing – original draft. **Hyunseung Kim:** Conceptualization, Methodology, Investigation, Visualization, Writing – original draft. **Gyoung-Ja Lee:** Methodology, Validation. **Han-Uk Lee:** Methodology, Validation. **Sang Gu Lee:** Methodology, Validation. **Chang-yeon Baek:** Resources, Validation. **Min-Ku Lee:** Resources, Validation. **Jin-Ju Park:** Resources, Validation. **Qing Wang:** Resources, Validation. **Sung Beom Cho:** Conceptualization, Writing – review & editing, Supervision, Resources, Funding acquisition. **Chang Kyu Jeong:** Conceptualization, Writing – review & editing, Supervision, Resources, Funding acquisition. **Kwi-il Park:** Conceptualization, Writing – review & editing, Supervision, Resources, Funding acquisition, Project administration.

Declaration of Competing Interest

The authors declare that they have no known competing financial interests or personal relationships that could have appeared to influence the work reported in this paper.

Acknowledgments

Yeon-gyu Kim and Hyunseung Kim contributed equally to this work. This research was supported by the Basic Science Research Program of the National Research Foundation of Korea, funded by the Ministry of Science and ICT (NRF-2021R1A4A2001658, 2019R1F1A1058554, 2019R1C1C1002571) and the Ministry of Education (NRF-2019R1I1A2A01057073). The computations were carried out using resources from Korea Supercomputing Center (KSC-2020-CRE-0023).

Appendix A. Supporting information

Supplementary data associated with this article can be found in the online version at doi:10.1016/j.nanoen.2021.106469.

References

- [1] K.-I. Park, J.H. Son, G.-T. Hwang, C.K. Jeong, J. Ryu, M. Koo, I. Choi, S.H. Lee, M. Byun, Z.L. Wang, K.J. Lee, Highly-efficient, flexible piezoelectric PZT thin film nanogenerator on plastic substrates, *Adv. Mater.* 26 (2014) 2514–2520, <https://doi.org/10.1002/adma.201305659>.
- [2] S. Park, J. Park, Y.-g. Kim, S. Bae, T.-W. Kim, K.-I. Park, B.H. Hong, C.K. Jeong, S.-K. Lee, Laser-directed synthesis of strain-induced crumpled MoS₂ structure for enhanced triboelectrification toward haptic sensors, *Nano Energy* 78 (2020), 105266, <https://doi.org/10.1016/j.nanoen.2020.105266>.
- [3] A. Sohn, J.H. Lee, H.-J. Yoon, H.H. Lee, S.-W. Kim, Self-boosted power generation of triboelectric nanogenerator with glass transition by friction heat, *Nano Energy* 74 (2020), 104840, <https://doi.org/10.1016/j.nanoen.2020.104840>.
- [4] K.-I. Park, M. Lee, Y. Liu, S. Moon, G.-T. Hwang, G. Zhu, J.E. Kim, S.O. Kim, D. K. Kim, Z.L. Wang, K.J. Lee, Flexible nanocomposite generator made of BaTiO₃ nanoparticles and graphitic carbons, *Adv. Mater.* 24 (2012) 2999–3004, <https://doi.org/10.1002/adma.201200105>.
- [5] J.H. Park, H.E. Lee, C.K. Jeong, D.H. Kim, S.K. Hong, K.-I. Park, K.J. Lee, Self-powered flexible electronics beyond thermal limits, *Nano Energy* 56 (2019) 531–546, <https://doi.org/10.1016/j.nanoen.2018.11.077>.
- [6] H. Cui, R. Hensleigh, D. Yao, D. Maurya, P. Kumar, M.G. Kang, S. Priya, X. (Rayne) Zheng, Three-dimensional printing of piezoelectric materials with designed anisotropy and directional response, *Nat. Mater.* 18 (2019) 234–241, <https://doi.org/10.1038/s41563-018-0268-1>.
- [7] D. Karpov, Z. Liu, T.D.S. Rolo, R. Harder, P.V. Balachandran, D. Xue, T. Lookman, E. Fohtung, Three-dimensional imaging of vortex structure in a ferroelectric nanoparticle driven by an electric field, *Nat. Commun.* 8 (2017) 280, <https://doi.org/10.1038/s41467-017-00318-9>.
- [8] M.H. Frey, D.A. Payne, Grain-size effect on structure and phase transformations for barium titanate, *Phys. Rev. B* 54 (1996) 3158–3168, <https://doi.org/10.1103/PhysRevB.54.3158>.
- [9] Z. Zhao, V. Buscaglia, M. Viviani, M.T. Buscaglia, L. Mitoseriu, A. Testino, M. Nygren, M. Johnsson, P. Nanni, Grain-size effects on the ferroelectric behavior of dense nanocrystalline BaTiO₃ ceramics, *Phys. Rev. B* 70 (2004), 024107, <https://doi.org/10.1103/PhysRevB.70.024107>.
- [10] A.N. Morozovska, I.S. Golovina, S.V. Lemishko, A.A. Andriiko, S.A. Khainakov, E. A. Eliseev, Effect of Vegard strains on the extrinsic size effects in ferroelectric nanoparticles, *Phys. Rev. B* 90 (2014), 214103, <https://doi.org/10.1103/PhysRevB.90.214103>.
- [11] C. Baek, J.E. Wang, S. Ryu, J.-H. Kim, C.K. Jeong, K.-I. Park, D.K. Kim, Facile hydrothermal synthesis of BaZr_xTi_{1-x}O₃ nanoparticles and their application to a lead-free nanocomposite generator, *RSC Adv.* 7 (2017) 2851–2856, <https://doi.org/10.1039/C6RA26285F>.
- [12] Y. Saito, H. Takao, T. Tani, T. Nonoyama, K. Takatori, T. Homma, T. Nagaya, M. Nakamura, Lead-free piezoceramics, *Nature* 432 (2004) 84–87, <https://doi.org/10.1038/nature03028>.
- [13] K.-I. Park, C.K. Jeong, J. Ryu, G.-T. Hwang, K.J. Lee, Flexible and large-area nanocomposite generators based on lead zirconate titanate particles and carbon nanotubes, *Adv. Energy Mater.* 3 (2013) 1539–1544, <https://doi.org/10.1002/aenm.201300458>.
- [14] Y. Sun, J. Chen, X. Li, Y. Lu, S. Zhang, Z. Cheng, Flexible piezoelectric energy harvester/sensor with high voltage output over wide temperature range, *Nano Energy* 61 (2019) 337–345, <https://doi.org/10.1016/j.nanoen.2019.04.055>.
- [15] S. Park, M. Peddigari, J.H. Kim, E. Kim, G.-T. Hwang, J.-W. Kim, C.-W. Ahn, J.-J. Choi, B.-D. Hahn, J.-H. Choi, W.-H. Yoon, D.-S. Park, K.-I. Park, C.K. Jeong, J. W. Lee, Y. Min, Selective phase control of dopant-free potassium sodium niobate perovskites in solution, *Inorg. Chem.* 59 (2020) 3042–3052, <https://doi.org/10.1021/acs.inorgchem.9b03385>.

- [16] C.K. Jeong, Toward bioimplantable and biocompatible flexible energy harvesters using piezoelectric ceramic materials, *MRS Commun.* 10 (2020) 365–378, <https://doi.org/10.1557/mrc.2020.48>.
- [17] Y. Zhang, H. Kim, Q. Wang, W. Jo, A.I. Kingon, S.H. Kim, C.K. Jeong, Progress in lead-free piezoelectric nanofiller materials and related composite nanogenerator devices, *Nanoscale Adv.* 2 (2020) 3131–3149, <https://doi.org/10.1039/c9na00809h>.
- [18] G.-J. Lee, M.-K. Lee, J.-J. Park, D.Y. Hyeon, C.K. Jeong, K.-I. Park, Piezoelectric energy harvesting from two-dimensional boron nitride nanoflakes, *ACS Appl. Mater. Interfaces* 11 (2019) 37920–37926, <https://doi.org/10.1021/acsami.9b12187>.
- [19] S.M. Kogan, Piezoelectric effect during inhomogeneous deformation and acoustic scattering of carriers in crystals, *Sov. Phys. -Solid State* 5 (1964) 2069–2070.
- [20] V.L. Indenbom, E.B. Loginov, M.A. Osipov, Flexoelectric effect and crystal-structure, *Kristallografiya* 26 (1981) 1157–1162.
- [21] L.E. Cross, Flexoelectric effects: charge separation in insulating solids subjected to elastic strain gradients, *J. Mater. Sci.* 41 (2006) 53–63, <https://doi.org/10.1007/s10853-005-5916-6>.
- [22] P. Zubko, G. Catalan, A. Buckley, P.R.L. Welche, J.F. Scott, Strain-gradient-induced polarization in SrTiO₃ single Crystals, *Phys. Rev. Lett.* 99 (2007) 167601, <https://doi.org/10.1103/PhysRevLett.99.167601>.
- [23] G. Catalan, A. Lubk, A.H.G. Vlooswijk, E. Snoeck, C. Magen, A. Janssens, G. Rispens, G. Rijnders, D.H.A. Blank, B. Noheda, Flexoelectric rotation of polarization in ferroelectric thin films, *Nat. Mater.* 10 (2011) 963–967, <https://doi.org/10.1038/nmat3141>.
- [24] D. Lee, A. Yoon, S.Y. Jang, J.-G. Yoon, J.-S. Chung, M. Kim, J.F. Scott, T.W. Noh, Giant flexoelectric effect in ferroelectric epitaxial thin films, *Phys. Rev. Lett.* 107 (2011) 057602, <https://doi.org/10.1103/PhysRevLett.107.057602>.
- [25] H. Lu, C.-W. Bark, D. Esque de los Ojos, J. Alcala, C.B. Eom, G. Catalan, A. Gruverman, Mechanical writing of ferroelectric polarization, *Science* 336 (2012) 59–61, <https://doi.org/10.1126/science.1218693>.
- [26] T.D. Nguyen, S. Mao, Y.-W. Yeh, P.K. Purohit, M.C. McAlpine, Nanoscale flexoelectricity, *Adv. Mater.* 25 (2013) 946–974, <https://doi.org/10.1002/adma.201203852>.
- [27] U.K. Bhaskar, N. Banerjee, A. Abdollahi, Z. Wang, D.G. Schlom, G. Rijnders, G. Catalan, A flexoelectric microelectromechanical system on silicon, *Nat. Nanotechnol.* 11 (2016) 263–266, <https://doi.org/10.1038/nano.2015.260>.
- [28] Y.L. Tang, Y.L. Zhu, Y. Liu, Y.J. Wang, X.L. Ma, Giant linear strain gradient with extremely low elastic energy in a perovskite nanostructure array, *Nat. Commun.* 8 (2017) 15994, <https://doi.org/10.1038/ncomms15994>.
- [29] M.-M. Yang, D.J. Kim, M. Alexe, Flexo-photovoltaic effect, *Science* 360 (2018) 904–907, <https://doi.org/10.1126/science.aan3256>.
- [30] G. Catalan, B. Noheda, J. McAneney, L.J. Sinnamon, J.M. Gregg, Strain gradients in epitaxial ferroelectrics, *Phys. Rev. B* 72 (2005) 020102, <https://doi.org/10.1103/PhysRevB.72.020102>.
- [31] B.C. Jeon, D. Lee, M.H. Lee, S.M. Yang, S.C. Chae, T.K. Song, S.D. Bu, J.-S. Chung, J.-G. Yoon, T.W. Noh, Flexoelectric effect in the reversal of self-polarization and associated changes in the electronic functional properties of BiFeO₃ thin films, *Adv. Mater.* 25 (2013) 5643–5649, <https://doi.org/10.1002/adma.201301601>.
- [32] K. Chu, B.-K. Jang, J.H. Sung, Y.A. Shin, E.-S. Lee, K. Song, J.H. Lee, C.-S. Woo, S. J. Kim, S.-Y. Choi, T.Y. Koo, Y.-H. Kim, S.-H. Oh, M.-H. Jo, C.-H. Yang, Enhancement of the anisotropic photocurrent in ferroelectric oxides by strain gradients, *Nat. Nanotechnol.* 10 (2015) 972–979, <https://doi.org/10.1038/nano.2015.191>.
- [33] G. Catalan, L.J. Sinnamon, J.M. Gregg, The effect of flexoelectricity on the dielectric properties of inhomogeneously strained ferroelectric thin films, *J. Phys. Condens. Matter* 16 (2004) 2253–2264, <https://doi.org/10.1088/0953-8984/16/13/006>.
- [34] K.J. Choi, Enhancement of ferroelectricity in strained BaTiO₃ thin films, *Science* 306 (2004) 1005–1009, <https://doi.org/10.1126/science.1103218>.
- [35] R.V.K. Mangalam, J. Karthik, A.R. Damodaran, J.C. Agar, L.W. Martin, Unexpected crystal and domain structures and properties in compositionally graded PbZr 1-x Ti x O 3 thin films, *Adv. Mater.* 25 (2013) 1761–1767, <https://doi.org/10.1002/adma.201204240>.
- [36] J.C. Agar, A.R. Damodaran, M.B. Okatan, J. Kacher, C. Gammer, R.K. Vasudevan, S. Pandya, L.R. Dedon, R.V.K. Mangalam, G.A. Velarde, S. Jesse, N. Balke, A. M. Minor, S.V. Kalinin, L.W. Martin, Highly mobile ferroelastic domain walls in compositionally graded ferroelectric thin films, *Nat. Mater.* 15 (2016) 549–556, <https://doi.org/10.1038/nmat4567>.
- [37] J.E. Wang, C. Baek, Y.H. Jung, D.K. Kim, Surface-to-core structure evolution of gradient BaTiO₃-Ba_{1-x}TiO₃ core-shell nanoparticles, *Appl. Surf. Sci.* 487 (2019) 278–284, <https://doi.org/10.1016/j.apsusc.2019.05.071>.
- [38] U. Manzoor, D.K. Kim, Synthesis of nano-sized barium titanate powder by solid-state reaction between barium carbonate and titania, *J. Mater. Sci. Technol.* 23 (2007) 655–658.
- [39] G. Kresse, J. Furthmüller, Efficient iterative schemes for ab initio total-energy calculations using a plane-wave basis set, *Phys. Rev. B* 54 (1996) 11169–11186, <https://doi.org/10.1103/PhysRevB.54.11169>.
- [40] P.E. Blöchl, Projector augmented-wave method, *Phys. Rev. B* 50 (1994) 17953–17979, <https://doi.org/10.1103/PhysRevB.50.17953>.
- [41] J.P. Perdew, K. Burke, M. Ernzerhof, Generalized gradient approximation made simple, *Phys. Rev. Lett.* 77 (1996) 3865–3868, <https://doi.org/10.1103/PhysRevLett.77.3865>.
- [42] A. Zunger, S.-H. Wei, L.G. Ferreira, J.E. Bernard, Special quasirandom structures, *Phys. Rev. Lett.* 65 (1990) 353–356, <https://doi.org/10.1103/PhysRevLett.65.353>.
- [43] A. van de Walle, M. Asta, G. Ceder, The alloy theoretic automated toolkit: a user guide, *Calphad* 26 (2002) 539–553, [https://doi.org/10.1016/S0364-5916\(02\)80006-2](https://doi.org/10.1016/S0364-5916(02)80006-2).
- [44] H.W. Kim, H. Ko, Y.-C. Chung, S.B. Cho, Heterostructural phase diagram of Ga₂O₃-based solid solution with Al₂O₃, *J. Eur. Ceram. Soc.* 41 (2021) 611–616, <https://doi.org/10.1016/j.jeurceramsoc.2020.08.067>.
- [45] S. Baroni, S. de Gironcoli, A. Dal Corso, P. Giannozzi, Phonons and related crystal properties from density-functional perturbation theory, *Rev. Mod. Phys.* 73 (2001) 515–562, <https://doi.org/10.1103/RevModPhys.73.515>.
- [46] A. Marmier, Z.A.D. Lethbridge, R.I. Walton, C.W. Smith, S.C. Parker, K.E. Evans, ELAM: a computer program for the analysis and representation of anisotropic elastic properties, *Comput. Phys. Commun.* 181 (2010) 2102–2115, <https://doi.org/10.1016/j.cpc.2010.08.033>.
- [47] Y. Yin, Formation of hollow nanocrystals through the nanoscale kirkendall effect, *Science* 304 (2004) 711–714, <https://doi.org/10.1126/science.1096566>.
- [48] J. Li, J. Camardese, R. Shunmugamurthi, S. Glazier, Z. Lu, J.R. Dahn, Synthesis and characterization of the lithium-rich core–shell cathodes with low irreversible capacity and mitigated voltage fade, *Chem. Mater.* 27 (2015) 3366–3377, <https://doi.org/10.1021/acscchemmater.5b00617>.
- [49] H.D.B. Jenkins, K.P. Thakur, Reappraisal of thermochemical radii for complex ions, *J. Chem. Educ.* 56 (1979) 576, <https://doi.org/10.1021/ed056p576>.
- [50] A.N. Morozovska, E.A. Eliseev, A.K. Tagantsev, S.L. Bravina, L.-Q. Chen, S. V. Kalinin, Thermodynamics of electromechanically coupled mixed ionic-electronic conductors: deformation potential, Vegard strains, and flexoelectric effect, *Phys. Rev. B* 83 (2011), 195313, <https://doi.org/10.1103/PhysRevB.83.195313>.
- [51] E.A. Eliseev, A.N. Morozovska, M.D. Glinchuk, R. Blinc, Spontaneous flexoelectric/flexomagnetic effect in nanoferroics, *Phys. Rev. B* 79 (2009), 165433, <https://doi.org/10.1103/PhysRevB.79.165433>.
- [52] M.S. Majdoub, P. Sharma, T. Cagin, Enhanced size-dependent piezoelectricity and elasticity in nanostructures due to the flexoelectric effect, *Phys. Rev. B* 77 (2008), 125424, <https://doi.org/10.1103/PhysRevB.77.125424>.
- [53] Y. Qi, J. Kim, T.D. Nguyen, B. Lisko, P.K. Purohit, M.C. McAlpine, Enhanced piezoelectricity and stretchability in energy harvesting devices fabricated from buckled PZT ribbons, *Nano Lett.* 11 (2011) 1331–1336, <https://doi.org/10.1021/nl104412b>.
- [54] Y. Chung, C. Yang, J. Lee, G.H. Wu, J.M. Wu, Coupling effect of piezo–flexocatalytic hydrogen evolution with hybrid 1T- and 2H-phase few-layered MoSe₂ nanosheets, *Adv. Energy Mater.* 10 (2020), 2002082, <https://doi.org/10.1002/aenm.202002082>.
- [55] T. Hoshina, S. Wada, Y. Kuroiwa, T. Tsurumi, Composite structure and size effect of barium titanate nanoparticies, *Appl. Phys. Lett.* 93 (2008), 192914, <https://doi.org/10.1063/1.3027067>.
- [56] B. Jiang, J. Icozzetti, L. Zhao, H. Zhang, Y.-W. Harn, Y. Chen, Z. Lin, Barium titanate at the nanoscale: controlled synthesis and dielectric and ferroelectric properties, *Chem. Soc. Rev.* 48 (2019) 1194–1228, <https://doi.org/10.1039/C8CS00583D>.
- [57] L. Hu, N. Yan, Q. Chen, P. Zhang, H. Zhong, X. Zheng, Y. Li, X. Hu, Fabrication based on the Kirkendall effect of Co₃O₄ porous nanocages with extraordinarily high capacity for lithium storage, *Chem. - Eur. J.* 18 (2012) 8971–8977, <https://doi.org/10.1002/chem.201200770>.
- [58] L. Höglund, J. Ågren, Analysis of the Kirkendall effect, marker migration and pore formation, *Acta Mater.* 49 (2001) 1311–1317, [https://doi.org/10.1016/S1359-6454\(01\)00054-4](https://doi.org/10.1016/S1359-6454(01)00054-4).
- [59] A. Li, C. Ge, P. Lü, D. Wu, S. Xiong, N. Ming, Fabrication and electrical properties of sol-gel derived BaTiO₃ films with metallic LaNiO₃ electrode, *Appl. Phys. Lett.* 70 (1997) 1616–1618, <https://doi.org/10.1063/1.118633>.
- [60] S. Jesse, H.N. Lee, S.V. Kalinin, Quantitative mapping of switching behavior in piezoresponce force microscopy, *Rev. Sci. Instrum.* 77 (2006), 073702, <https://doi.org/10.1063/1.2214699>.
- [61] B.J. Rodriguez, S. Jesse, A.P. Baddorf, T. Zhao, Y.H. Chu, R. Ramesh, E.A. Eliseev, A.N. Morozovska, S.V. Kalinin, Spatially resolved mapping of ferroelectric switching behavior in self-assembled multiferroic nanostructures: strain, size, and interface effects, *Nanotechnology* 18 (2007), 405701, <https://doi.org/10.1088/0957-4484/18/40/405701>.
- [62] M. Stewart, M.G. Cain, Direct piezoelectric measurement: the berlincourt method, in: *Characterisation Ferroelectr. Bulk Mater. Thin Film*, Springer, US, 2014, pp. 37–64, https://doi.org/10.1007/978-1-4020-9311-1_3.
- [63] Z. Deng, Y. Dai, W. Chen, X. Pei, J. Liao, Synthesis and characterization of bowl-like single-crystalline BaTiO₃ nanoparticles, *Nanoscale Res. Lett.* 5 (2010) 1217–1221, <https://doi.org/10.1007/s11671-010-9629-7>.

- [64] P. Bharathi, P. Thomas, K.B.R. Varma, Piezoelectric properties of individual nanocrystallites of Ba 0.85 Ca 0.15 Zr 0.1 Ti 0.9 O 3 obtained by oxalate precursor route, *J. Mater. Chem. C* 3 (2015) 4762–4770, <https://doi.org/10.1039/C5TC00530B>.
- [65] D. Mohanty, G.S. Chaubey, A. Yourdkhani, S. Adireddy, G. Caruntu, J.B. Wiley, Synthesis and piezoelectric response of cubic and spherical LiNbO₃ nanocrystals, *RSC Adv.* 2 (2012) 1913, <https://doi.org/10.1039/c2ra00628f>.
- [66] D. Carranza-Celis, A. Cardona-Rodríguez, J. Narváez, O. Moscoso-Londono, D. Muraca, M. Knobel, N. Ornelas-Soto, A. Reiber, J.G. Ramírez, Control of Multiferroic properties in BiFeO₃ nanoparticles, *Sci. Rep.* 9 (2019) 3182, <https://doi.org/10.1038/s41598-019-39517-3>.
- [67] R. Bhimireddi, B. Ponraj, K.B.R. Varma, Structural, optical, and piezoelectric response of lead-free Ba 0.95 Mg 0.05 Zr 0.1 Ti 0.9 O 3 nanocrystalline powder, *J. Am. Ceram. Soc.* 99 (2016) 896–904, <https://doi.org/10.1111/jace.14018>.
- [68] C. Chao, Z. Ren, S. Yin, S. Gong, X. Yang, G. Xu, X. Li, G. Shen, G. Han, Hydrothermal synthesis of ferroelectric PbTiO₃ nanoparticles with dominant {001} facets by titanate nanostructure, *CrystEngComm* 15 (2013) 8036, <https://doi.org/10.1039/c3ce41248b>.
- [69] Y. Takada, K.I. Mimura, K. Kato, Fabrication and piezoelectric properties of Pb(Zr, Ti)O₃ cubes synthesized by hydrothermal method, *J. Ceram. Soc. Jpn.* 126 (2018) 326–330, <https://doi.org/10.2109/jcersj2.17248>.
- [70] X. Chen, X. Li, J. Shao, N. An, H. Tian, C. Wang, T. Han, L. Wang, B. Lu, High-performance piezoelectric nanogenerators with imprinted P(VDF-TrFE)/BaTiO₃ nanocomposite micropillars for self-powered flexible sensors, *Small* 13 (2017), 1604245, <https://doi.org/10.1002/smll.201604245>.
- [71] S. Ye, C. Cheng, X. Chen, X. Chen, J. Shao, J. Zhang, H. Hu, H. Tian, X. Li, L. Ma, W. Jia, High-performance piezoelectric nanogenerator based on microstructured P(VDF-TrFE)/BNNTs composite for energy harvesting and radiation protection in space, *Nano Energy* 60 (2019) 701–714, <https://doi.org/10.1016/j.nanoen.2019.03.096>.
- [72] E. Kar, N. Bose, B. Dutta, S. Banerjee, N. Mukherjee, S. Mukherjee, 2D SnO₂ nanosheet/PVDF composite based flexible, self-cleaning piezoelectric energy harvester, *Energy Convers. Manag.* 184 (2019) 600–608, <https://doi.org/10.1016/j.enconman.2019.01.073>.
- [73] H. Su, X. Wang, C. Li, Z. Wang, Y. Wu, J. Zhang, Y. Zhang, C. Zhao, J. Wu, H. Zheng, Enhanced energy harvesting ability of polydimethylsiloxane-BaTiO₃-based flexible piezoelectric nanogenerator for tactile imitation application, *Nano Energy* 83 (2021), 105809, <https://doi.org/10.1016/j.nanoen.2021.105809>.
- [74] Y. Zhang, C.K. Jeong, J. Wang, H. Sun, F. Li, G. Zhang, L.-Q. Chen, S. Zhang, W. Chen, Q. Wang, Flexible energy harvesting polymer composites based on biofilm-templated 3-dimensional interconnected piezoceramics, *Nano Energy* 50 (2018) 35–42, <https://doi.org/10.1016/j.nanoen.2018.05.025>.
- [75] K. kumar Sappati, S. Bhadra, 0–3 Barium Titanate-PDMS Flexible Film for Tactile Sensing, in: 2020 IEEE Int. Instrum. Meas. Technol. Conf., IEEE, 2020: pp. 1–6. (<https://doi.org/10.1109/I2MTC43012.2020.9128512>).
- [76] Y. Zhang, M. Wu, Q. Zhu, F. Wang, H. Su, H. Li, C. Diaoy, H. Zheng, Y. Wu, Z. L. Wang, Performance enhancement of flexible piezoelectric nanogenerator via doping and rational 3D structure design for self-powered mechanosensational system, *Adv. Funct. Mater.* 29 (2019), 1904259, <https://doi.org/10.1002/adfm.201904259>.
- [77] C. Luo, S. Hu, M. Xia, P. Li, J. Hu, G. Li, H. Jiang, W. Zhang, A flexible lead-free BaTiO₃/PDMS/C composite nanogenerator as a piezoelectric energy harvester, *Energy Technol.* 6 (2018) 922–927, <https://doi.org/10.1002/ente.201700756>.
- [78] M. Wu, T. Zheng, H. Zheng, J. Li, W. Wang, M. Zhu, F. Li, G. Yue, Y. Gu, J. Wu, High-performance piezoelectric-energy-harvester and self-powered mechanosensing using lead-free potassium-sodium niobate flexible piezoelectric composites, *J. Mater. Chem. A* 6 (2018) 16439–16449, <https://doi.org/10.1039/C8TA05887C>.
- [79] W. Wang, J. Zhang, Y. Zhang, F. Chen, H. Wang, M. Wu, H. Li, Q. Zhu, H. Zheng, R. Zhang, Remarkably enhanced hybrid piezo/triboelectric nanogenerator via rational modulation of piezoelectric and dielectric properties for self-powered electronics, *Appl. Phys. Lett.* 116 (2020), 023901, <https://doi.org/10.1063/1.5134100>.
- [80] A.A. Khan, G. Huang, M.M. Rana, N. Mei, M. Biondi, S. Rassel, N. Tanguy, B. Sun, Z. Leonenko, N. Yan, C. Wang, S. Xu, D. Ban, Superior transverse piezoelectricity in organic-inorganic hybrid perovskite nanorods for mechanical energy harvesting, *Nano Energy* 86 (2021), 106039, <https://doi.org/10.1016/j.nanoen.2021.106039>.
- [81] C.K. Jeong, K.-I. Park, J. Ryu, G.-T. Hwang, K.J. Lee, Large-area and flexible lead-free nanocomposite generator using alkaline niobate particles and metal nanorod filler, *Adv. Funct. Mater.* 24 (2014) 2620–2629, <https://doi.org/10.1002/adfm.201303484>.
- [82] K.-I. Park, S. Bin Bae, S.H. Yang, H.I. Lee, K. Lee, S.J. Lee, Lead-free BaTiO₃ nanowires-based flexible nanocomposite generator, *Nanoscale* 6 (2014) 8962–8968, <https://doi.org/10.1039/C4NR02246C>.
- [83] H. Park, D.Y. Hyeon, M. Jung, K.-I. Park, J. Park, Piezoelectric BaTiO₃ microclusters and embossed ZnSnO₃ microspheres-based monolayer for highly-efficient and flexible composite generator, *Compos. Part B: Eng.* 203 (2020), 108476, <https://doi.org/10.1016/j.compositesb.2020.108476>.
- [84] W. Zhu, J.Y. Fu, N. Li, L. Cross, Piezoelectric composite based on the enhanced flexoelectric effects, *Appl. Phys. Lett.* 89 (2006), 192904, <https://doi.org/10.1063/1.2382740>.
- [85] D. Lee, T.W. Noh, Giant flexoelectric effect through interfacial strain relaxation, *Philos. Trans. R. Soc. A Math. Phys. Eng. Sci.* 370 (2012) 4944–4957, <https://doi.org/10.1098/rsta.2012.0200>.
- [86] Y. Hao, X. Wang, K. Bi, J. Zhang, Y. Huang, L. Wu, P. Zhao, K. Xu, M. Lei, L. Li, Significantly enhanced energy storage performance promoted by ultimate sized ferroelectric BaTiO₃ fillers in nanocomposite films, *Nano Energy* 31 (2017) 49–56, <https://doi.org/10.1016/j.nanoen.2016.11.008>.
- [87] P.-J. Wang, D. Zhou, H.-H. Guo, W.-F. Liu, J.-Z. Su, M.-S. Fu, C. Singh, S. Trukhanov, A. Trukhanov, Ultrahigh enhancement rate of the energy density of flexible polymer nanocomposites using core-shell BaTiO₃@MgO structures as the filler, *J. Mater. Chem. A* 8 (2020) 11124–11132, <https://doi.org/10.1039/DOTA03304A>.
- [88] Z. Li, L.A. Fredin, P. Tewari, S.A. DiBenedetto, M.T. Lanagan, M.A. Ratner, T. J. Marks, In situ catalytic encapsulation of core-shell nanoparticles having variable shell thickness: dielectric and energy storage properties of high-permittivity metal oxide nanocomposites, *Chem. Mater.* 22 (2010) 5154–5164, <https://doi.org/10.1021/cm1009493>.
- [89] D. Yu, N. Xu, L. Hu, Q. Zhang, H. Yang, Nanocomposites with BaTiO₃–SrTiO₃ hybrid fillers exhibiting enhanced dielectric behaviours and energy-storage densities, *J. Mater. Chem. C* 3 (2015) 4016–4022, <https://doi.org/10.1039/C4TC02972K>.
- [90] W. Ma, L.E. Cross, Observation of the flexoelectric effect in relaxor Pb(Mg_{1/3}Nb_{2/3})O₃ ceramics, *Appl. Phys. Lett.* 78 (2001) 2920–2921, <https://doi.org/10.1063/1.1356444>.
- [91] W. Ma, Flexoelectric charge separation and size dependent piezoelectricity in dielectric solids, *Phys. Status Solidi* 247 (2010) 213–218, <https://doi.org/10.1002/pssb.200945394>.
- [92] R. Yang, Y. Qin, L. Dai, Z.L. Wang, Power generation with laterally packaged piezoelectric fine wires, *Nat. Nanotechnol.* 4 (2009) 34–39, <https://doi.org/10.1038/nano.2008.314>.
- [93] K.-I. Park, S. Xu, Y. Liu, G.-T. Hwang, S.-J.L. Kang, Z.L. Wang, K.J. Lee, Piezoelectric BaTiO₃ thin film nanogenerator on plastic substrates, *Nano Lett.* 10 (2010) 4939–4943, <https://doi.org/10.1021/nl102959k>.
- [94] S.S. Ham, G.-J. Lee, D.Y. Hyeon, Y.-g. Kim, Y. Lim, M.-K. Lee, J.-J. Park, G.-T. Hwang, S. Yi, C.K. Jeong, K.-I. Park, Kinetic motion sensors based on flexible and lead-free hybrid piezoelectric composite energy harvesters with nanowires-embedded electrodes for detecting articular movements, *Compos. Part B: Eng.* 212 (2021), 108705, <https://doi.org/10.1016/j.compositesb.2021.108705>.
- [95] G.-J. Lee, M.-K. Lee, J.-J. Park, D.Y. Hyeon, C.K. Jeong, K.-I. Park, Piezoelectric energy harvesting from two-dimensional boron nitride nanoflakes, *ACS Appl. Mater. Interfaces* 11 (2019) 37920–37926, <https://doi.org/10.1021/acsami.9b12187>.

Yeon-gyu Kim is a M.S. candidate in the Department of Materials Science and Metallurgical Engineering at Kyungpook National University. He received his B.S. degree in the Department of Materials Science and Metallurgical Engineering from Kyungpook National University in 2020. His research interests include synthesis/characterization of ferro/piezoelectric nanomaterials and mechanical energy harvesting systems.



Hyunseung Kim is a M.S. candidate in the Department of Energy Storage/Conversion Engineering of Graduate School at Jeonbuk National University. He received his B.S. degree in the Division of Advanced Materials Engineering, Major of Electronic Materials Engineering from Jeonbuk National University in 2020. His research interests include piezoelectrics & dielectrics, eco-friendly composites including biopolymers





Dr. Sung Beom Cho is currently Senior Researcher in Korea Institute of Ceramic Engineering and Technology (KICET). He received B.S. degree in physics and materials science (2011), and Ph.D. in materials science (2017) from Hanyang University. He has extensive experience in computational modeling on materials and devices using first-principle calculation, multi-physics finite element analysis, and machine learning. His recent activities include electroceramics, energy harvester, functional semiconductor design, and the digital transformation of the materials industry.



Prof. Kwi-il Park is a professor in the Department of Materials Science and Metallurgical Engineering at Kyungpook National University. Prof. Park received his Ph.D. in Materials Science and Engineering at Korea Advanced Institute of Science and Technology (KAIST). He was previously a senior researcher at Korea Agency for Defense Development from 2014 to 2015 and a faculty member at Gyeongnam National University of Science and Technology from 2015 to 2018. His research interests include the synthesis of high-performance piezoelectric/thermoelectric nanomaterials and development of flexible/stretchable energy harvester based on organic/inorganic materials.



Prof. Chang Kyu Jeong is currently a professor in Jeonbuk National University, Korea. He was born in Seoul and received his B.S. degree in Materials Science and Engineering from Hanyang University. He holds his M.S. and Ph.D. degrees from the Department of Materials Science and Engineering, Korea Advanced Institute of Science and Technology (KAIST). Before the current affiliation, he was employed as a postdoctoral scholar in The Pennsylvania State University, USA. At Jeonbuk National University, his current research topics are biological and environmental electronic devices for energy and sensor applications using ferroelectric, piezoelectric, and dielectric materials.